A stable and moderate nitrate pool in largely anoxic Mesoproterozoic oceans and implications for eukaryote evolution

Jia Tao[a, b], Jinchuan Zhang[a, b*], Yang Liu[a, b*], Eva E. Stüeken[c], Zhe Dong[d], Miao Shi[e], Peng Li[f], Qingxi Zhang[f], Simon W. Poulton[g]

[a] *School of Energy resources, China University of Geosciences (Beijing), Beijing 100083, China.*
[b] *Key Laboratory of Strategy Evaluation for Shale Gas of Ministry of Land and Resources, China University of Geosciences (Beijing), Beijing, 100083, China.*
[c] *School of Earth and Environmental Sciences, University of St. Andrews, St. Andrews KY16 9AL, United Kingdom.*
[d] *School of Earth Science, University of Bristol, Bristol, BS8 1QE, United Kingdom.*
[e] *School of gemology and materials science, Hebei GEO university, Shijiazhuang 050031, China.*
[f] *Hebei Province Coal Geological Exploration Institute, Xingtai 054000, China.*
[g] *School of Earth and Environment, University of Leeds, Leeds LS2 9JT, United Kingdom.*
Corresponding Author: yangliu@cugb.edu.cn and zhangjc@cugb.edu.cn

Abstract

The Mesoproterozoic (1.6–1.0 Ga) is a particularly important interval in Earth history that witnessed the initial radiation of eukaryotic life. Ocean anoxia and nutrient limitation has been invoked to explain the delayed expansion of more complex, multicellular eukaryotes during the Mesoproterozoic. However, pulsed oxygenation events and elevated nitrate availability have been identified in shallow marine settings. In deeper waters, however, nitrate availability and potential links to eukaryotic evolution remain poorly constrained. Here, we report an integrated geochemical study based on multiple proxies conducted on two new drill-core sections from the ~1460 Ma Hongshuizhuang Formation and the ~1380 Ma Xiamaling Formation, North China. Iron speciation and redox-sensitive trace element systematics suggest dominantly ferruginous to weakly euxinic water column conditions during deposition of both units. Our data are consistent with previous inferences of persistently anoxic deep water

conditions in Mesoproterozoic oceans. Exclusively positive $\delta^{15}N$ (+3.1 ± 0.8‰) values reveal the operation of partial denitrification in the water column, implying a relatively stable and moderate nitrate pool in offshore surface waters. Furthermore, a compilation of the Mesoproterozoic sedimentary $\delta^{15}N$ record suggests a global nearshore to offshore oceanic nitrate gradient, with minimal but still bioavailable nitrate in offshore environments. The overall size of the nitrate pool was therefore apparently smaller than that of eukaryote-dominated modern oceans. Coupling Mesoproterozoic sedimentary $\delta^{15}N$ data with fossil and biomarker records, we propose that this moderate level of nitrate may have been able to sustain a relatively low abundance of eukaryotic primary producers in the marine ecosystem, but was still not sufficient to trigger eukaryotic diversification and the rise of eukaryotes to ecological dominance.

Keywords: Ocean redox; Nitrate pool; Eukaryote evolution; Mesoproterozoic; North China

1. Introduction

The Mesoproterozoic (1.6–1.0 Ga) has long been viewed as a period of relative environmental and biological evolutionary stagnation, which has been frequently referred as 'the Boring Billion' (e.g., Brasier and Lindsay, 1998), or more recently, the 'Barren billion' (e.g., Young, 2013). It has been suggested that atmospheric oxygen concentration fell to a low, but uncertain, level immediately after the Lomagundi Event at ~2.2–2.1 Ga (Ossa Ossa et al., 2018) and remained low throughout the entire Mesoproterozoic (Planavsky et al., 2014; Cole et al., 2016). Correspondingly, multiple lines of evidence have suggested that the Mesoproterozoic oceans were redox stratified, with anoxic deeper waters overlain by shallower oxic waters and the occurrence of euxinia along some productive continental margins (Poulton et al., 2010; Planavsky et al., 2011; Poulton and Canfield, 2011; Luo et al., 2014; Doyle et al., 2018). In addition, this low oxygen Mesoproterozoic atmosphere–ocean ecosystem has been invoked to explain the delayed diversification of eukaryotes (e.g., Lyons et al., 2014; Reinhard et al., 2016). However, emerging evidence suggests that the redox state of the atmosphere–ocean system and biological evolution during the Mesoproterozoic may have been more dynamic than previously considered (e.g., Zhang et al., 2016; Zhu et al., 2016; Canfield et al., 2018; Zhang et al., 2018).

Studies conducted on geographically distinct sedimentary basins in this era indicate a shallow chemocline (Luo et al., 2014; Doyle et al., 2018) and spatiotemporal redox heterogeneity in the Mesoproterozoic ocean (Wang et al., 2020a). Some studies even provide evidence for apparent deepening of the chemocline and pulsed oxygenation events, notably in the ~1.56 Ga Yanliao basin, North China, coincident with the emergence of decimetre-scale, multicellular eukaryotic macrofossils (Zhu et al., 2016; Zhang et al., 2018; Shang et al., 2019; Luo et al., 2021), in the ~1.4 Ga Kyrpy Group, Russia (Sperling et al., 2014), in the ~1.4 Ga Yanliao basin, North China (Zhang et al., 2016), in the ~1380 Ma McArthur Basin, northern Australian (Yang et al., 2017),

and in the ~1.1 Ga El Mreiti Group, Mauritania (Gilleaudeau et al., 2016; Sheen et al., 2018). Furthermore, the possible development of modern-like, fully oxygenated deeper waters beneath an oxygen minimum zone (OMZ) has been suggested based on evidence from the ~1.4 Ga Xiamaling Formation, North China (Zhang et al., 2016). However, despite these episodes of Mesoproterozoic ocean oxygenation, there is no evidence for substantial continued evolution and diversification of eukaryotes after ~1.56 Ga.

The availability of bio-limiting nutrients, in particular nitrogen (N) and phosphorus (P), exerts a strong control on biological evolution (e.g., Anbar and Knoll, 2002; Brocks et al., 2017; Reinhard et al., 2017; Wang et al., 2018). For instance, nitrate limitation in deeper waters may have contributed to the absence of eukaryotic organisms in oxygenated peritidal environments in the ~1.5 Ga Bangemall basin (Koehler et al., 2017), suggesting that nitrate availability potentially exerted a control on eukaryotic evolution. A similar nearshore to offshore gradient in nitrate availability has been found in the Mesoproterozoic ~1.4 Ga Belt Supergroup, the ~1.5 Ga Bangemall, and the ~1.4–1.5 Ga Roper basins, which may have restricted eukaryotes to nearshore environments and limited their ability to diversify (Stüeken, 2013; Koehler et al., 2017). In the modern ocean, nitrogen limitation favors cyanobacteria over eukaryotic algae; however, it is unlikely that eukaryotic algae would be completely excluded even under extreme nitrogen limitation (e.g., Otero-Ferrer et al., 2018). Indeed, indicators for eukaryotic algae occur in the biomarker record from deep-water black shales in the ~1.4 Ga Xiamaling Fm (Zhang et al., 2021). Although the availability of fixed nitrogen may have been low in deeper offshore waters during the Mesoproterozoic, the extent of nitrogen limitation and its impact on eukaryotic evolution remain unclear.

The well-preserved Mesoproterozoic sedimentary sequence in North China has served as an important window into the evolution of the biosphere, atmosphere and ocean during this critical interval. In this study, we present iron (Fe) speciation, redox-sensitive trace element (RSE), and nitrogen isotope ($\delta^{15}N$) data for samples from two new drill-cores through the ~1460 Ma Hongshuizhuang (HSZ) Formation (Fm.) and the ~1380 Ma Xiamaling (XML) Fm., North China. We combine our new data with published geochemical data from globally correlative sections to explore variability in marine nitrogen availability in the Mesoproterozoic oceans and links to the evolution of eukaryotes during this period.

2. Geological setting

The Yanliao Basin is located in the northern part of the North China Craton (Fig. 1A and 1B). A thick (~9000 m) late Paleo- to Mesoproterozoic marine sedimentary succession was deposited in the Yanliao Basin (Li et al., 2013). The sedimentary sequence reflects continuous sedimentation, is weakly metamorphosed (below greenschist facies) and well-preserved (Luo et al., 2014). The overall package can be further subdivided into the Changcheng System (~1650–1600 Ma), the Jixian System (1600–1400 Ma), and an unnamed system (1400–1000 Ma) in ascending order (Fig. 1C; Li et al., 2014).

The HSZ and XML formations were deposited in the Mesoproterozoic and belong to the Jixian System and the Unnamed System, respectively. The HSZ Fm. rests unconformably on the Wumishan (WMS) Fm. and is overlain conformably by the Tieling (TL) Fm., which passes upwards into the XML Fm. Currently, there is no direct geochronological evidence for the age of the HSZ Fm., due to an absence of suitable units for radiometric dating (Cheng et al., 2020). Nevertheless, based on the zircon U-Pb SHRIMP ages of 1483 ± 13 Ma and 1487 ± 16 Ma from the underlying WMS Fm. (Li et al., 2014), and 1437 ± 21 Ma and 1439 ± 14 Ma from the overlying TL Fm. (Su et al., 2010; Li et al., 2014), the depositional age of the HSZ Fm. can be approximately constrained to between ~1470 Ma and ~1450 Ma. A number of high-precision age data for the XML Fm. have been obtained (e.g., 1384 ± 1.4 Ma and 1392 ± 1.0 Ma; Zhang et al., 2015), and in combination with an assumed average deposition rate (Wang et al., 2020a), the lower and upper ages of the XML Fm. are constrained at ~1400 Ma and ~1320 Ma, respectively.

Paleogeographic reconstructions show that the HSZ and XML formations are widely distributed in the Yanliao Basin, extending approximately 500 km from the northeast to the southwest (Shi et al., 2021). The depocenter of the HSZ Fm. is mainly located in the Xinglong and Kuancheng area (Ma et al., 2017), within which the HSZ Fm. can be divided into three members according to variations in lithology and sedimentary environment. The lower sub-unit (Member I) is mainly composed of alternating dolomitic shale and argillaceous dolomite, the middle sub-unit (Member II) is dominated by black shale containing some pyrite and marl lenses, and the upper sub-unit (Member III) consists of dolomite (Shi et al., 2021). The depocenter moved westward to the Huailai–Zhuolu areas during deposition of the XML Fm., and here the strata can be further divided into four members from the base to the top. Member I comprises silty shale, the color of which varies upwards, from greenish-yellow and light gray to gray, to dark gray, with locally recognizable Fe-rich sandstone and siltstone at its base. Member II consists of three lithological sub-units: the lower sub-unit is a set of greenish-grey glauconite-bearing sandstone and siltstone; the middle sub-unit is characterized by greenish shale which alternates with purplish shale with some carbonate lenticles; and the upper sub-unit is composed of greenish-grey shale interbedded with black shale. Member III typically consists of thick black shale and contains a few thin siliceous rock interlayers at its base. A gradual transition occurs upwards from Member III to Member IV, which comprises interbedded black and greenish shales with some carbonate concretions and lenticles (Wang et al., 2020a).

The samples for this study were taken from drill cores CQ-1 and CQ-2 in Chengde City, Hebei Province. The HSZ Fm. that occurs in CQ-1 (Fig. 1E) can be correlated with Member I and Member II of previously studied sections in the Jixian and Kuancheng areas (Shi et al., 2021). The XML Fm. encountered in CQ-2 (Fig. 1D) most likely represents Member III in the Huailai–Zhuolu area (Wang et al., 2020a). The absence of ripple marks, cross bedding and other sedimentary structures indicative of storm waves in our sample set indicates that the depositional setting was largely below storm wave base.

3. Materials and methods

A total of 86 drill-core samples were collected from drill core CQ-1 and drill core CQ-2, including 46 shale samples and 9 carbonate samples from the HSZ Fm., and 28 shale samples, 1 silty shale and 2 siltstone samples from the XML Fm. Prior to the geochemical analyses, drill-core samples were carefully cut with a water-cooled saw to remove visible veining, pyrite nodules or bands, and possible weathered surfaces. Approximately 200 g of remaining material from each sample was crushed to powder (~200 mesh) in an agate mortar to avoid metal and carbon contamination. All geochemical analyses were carried out in the State Key Laboratory of Biogeology and Environmental Geology at the China University of Geosciences (Wuhan).

Fe speciation analysis was conducted to reconstruct water column redox conditions. Four pools of highly reactive Fe (Fe_{HR}) were determined, including carbonate Fe (Fe_{carb}), ferric (oxyhydr)oxide Fe (Fe_{ox}), magnetite Fe (Fe_{mag}) and pyrite Fe (Fe_{py}). Fe_{py} was calculated stoichiometrically by the content of pyrite sulfur extracted following the chromium reduction method of Canfield et al. (1986). The other three Fe species, Fe_{carb}, Fe_{ox} and Fe_{mag}, were determined through an operationally-defined sequential extraction procedure (Poulton and Canfield, 2005). First, approximately 80 mg of sample powder was weighed into a 15 ml centrifuge tube and treated with 10 ml of 1 mol/L sodium acetate solution (pH = 4.5 with acetic acid), then the centrifuge tube was placed in a water bath shaker (50°C) for 48 h in order to extract Fe_{carb}. Second, the sample residue from the first step was dissolved in 10 ml of 50 g/L sodium dithionite and 0.2 mol/L sodium citrate mixed solution (pH = 4.8 with acetic acid), followed by shaking for 2 h at room temperature in order to extract Fe_{ox}. Finally, the sample residue from the second step was treated with 10 ml of a 0.17 mol/L oxalic acid and 0.2 mol/L ammonium oxalate solution for 6 h at room temperature in order to extract Fe_{mag}. All extraction solutions were diluted 100-fold with 2% HNO_3 before analysis by atomic absorption spectroscopy (AAS). The analytical precision for each fraction was within 5%, based on replicate analyses of the international Fe speciation standard, WHIT (Alcott et al., 2020).

For major element analysis, approximately 1 g of dried sample powder was mixed with 6 g lithium tetraborate, lithium metaborate and lithium fluoride, then the mixture was fused into glass disks at 1000°C and major element compositions were determined via X-ray fluorescence spectrometry (XRF-1800). For trace element analysis, approximately 50 mg of sample powder was first moistened with 1–2 drops of ultrapure water and then digested in 1 ml HNO_3 and 1 ml HF in a Teflon vessel. The liquid sample was subsequently placed into an oven and heated at 190°C for 48 h. After complete digestion, the sample was evaporated at 115°C on a hot plate to remove the concentrated acid, and the dried sample was subsequently dissolved in 1 ml HNO_3 and again evaporated to dryness. The resultant salt was re-digested in 3 ml of 30% HNO_3 and heated at 190°C in an oven for 12 h. Finally, the solution was decanted to a polyethylene bottle and diluted to 100 g with 2% nitric acid for trace element analysis using an Agilent 7700x inductively coupled plasma mass spectrometer (ICP-MS). Three international rock standards (BHVO-2, AGV-2, BCR-2) and two Chinese national

standards (GSR-5, GSR-6) were used to monitor analytical precision, which was better than 5% for the presented elements. RSE enrichment factors (EFs) were calculated as follows: $X_{EF} = (X/Al)_{sample}/(X/Al)_{AUCC}$, where X is the trace element of interest (e.g., Mo, U, V) and the subscripts 'sample' and 'AUCC' refer to the studied sample and average upper continental crust, respectively (McLennan, 2001).

Total organic carbon (TOC), total nitrogen (TN) and $\delta^{15}N$ values were analyzed following the procedures described in Du et al. (2021). Prior to analysis, sample powder was treated with 3 mol/L HCl for 24 h to remove inorganic carbon, and then the residue was thoroughly rinsed with 18.2 MΩ/cm deionized water and left to dry in a ventilated oven overnight. Approximately 200 mg of sample powder and 10 mg WO_3 were subsequently packed into a tin capsule for measurement of TOC and TN, using a Vario Macro Cube elemental analyzer (Elementar, Hanau, Germany). Analytical errors were less than 0.05 wt% based on replicate analyses of multiple samples. $\delta^{15}N$ values were analyzed using a Flash HT 2000 Plus and continuous-flow Delta V Advantage IRMS (Thermo Fisher Scientific). Briefly, 40–80 mg of dried carbonate-free sample powder and 10 mg of CuO were weighed into a tin capsule for nitrogen isotope analysis through online combustion at 1020°C, and an alkali lime trap was used to absorb CO_2 and H_2O to avoid interferences. $\delta^{15}N$ values are expressed in per mil (‰) relative to atmospheric N_2 ($\delta^{15}N$ = 0‰). Uncertainties determined by replicate analyses of two international standards (USGS40, $\delta^{15}N$ = –4.52‰; SANTIS-SA33802151, $\delta^{15}N$ = +4.32‰) were less than 0.5‰ for $\delta^{15}N$.

4. Results

Fe speciation, RSE concentrations, C-N abundances, and $\delta^{15}N$ values for the HSZ and XML formations are listed in Table S1 and illustrated in Figs. 2–4.

4.1 Fe speciation

The majority of samples analyzed in this study have total iron (Fe_T) contents well above 0.5 wt% (Table S1), which is the threshold commonly considered ideal for Fe speciation analysis (Clarkson et al., 2014). In the HSZ Fm., the Fe_{HR} pool is typically dominated by Fe_{py} (mean 70.7 ± 15.6%), followed by Fe_{carb} (mean 23.7 ± 13.3%), with low amounts of Fe_{ox} and Fe_{mag} (mean 3.2 ± 2.1% and 2.4 ± 3.1%, respectively; Fig. 2). Stratigraphically, Fe_{HR}/Fe_T ratios are consistently high, with an average value of 0.75 ± 0.11 (1σ) throughout the entire section (Fig. 3). Fe_{py}/Fe_{HR} ratios are similarly high, with relatively larger variation (mean 0.71 ± 0.16; Fig. 3). Specifically, Fe_{py}/Fe_{HR} ratios increase persistently from the bottom of the section and reach a peak value of 0.94 at 98 m, which is then followed by a gradual decline to 0.48, before rebounding to a value of 0.87 at 67 m. Above 67 m, Fe_{py}/Fe_{HR} ratios first show a two-step decrease to a minimum value of 0.39, but thereafter increase upwards to 0.77 and stabilize at a high level for the rest of the section (except for one value of 0.09 at 16.3 m).

Similarly, Fe_{py} (mean 61.9 ± 21.4%) and Fe_{carb} (mean 25.7 ± 21.2%) dominate the Fe_{HR} pool in the XML Fm., whereas Fe_{ox} and Fe_{mag} contents (mean 5.3 ± 1.8% and 7.1 ± 3.9%, respectively; Fig. 2) are slightly higher than in the HSZ Fm. Stratigraphically,

Fe_{HR}/Fe_T ratios (mean 0.56 ± 0.16) generally exceed 0.38, with one exception of 0.30 for the uppermost sample (Fig. 3). Fe_{py}/Fe_{HR} ratios show some scatter, ranging from 0.07 to 0.79, but mostly fall around 0.7, with no clear stratigraphic trend (Fig. 3).

4.2 RSE concentrations

The Mo concentrations of all investigated samples from the HSZ Fm. range from 0.001 ppm to 80.1 ppm, with a systematic increase towards an overall average value of 37.4 ± 12.9 ppm in the uppermost section. Conversely, RSE display overall moderate to strong enrichments relative to AUCC (Table S1), with a relatively consistent pattern of variation through the stratigraphy. Specifically, RSE EFs in the lower part of the section are more variable, with Mo_{EF} values varying from 0.01 to 28.0, U_{EF} varying from 1.3 to 4.8, V_{EF} varying from 0.11 to 5.3, and Mo/U ratios varying from 0.002 to 7.9. RSE EFs tend to increase up-section (mean 20.1 ± 17.7 for Mo_{EF}, 3.2 ± 1.3 for U_{EF}, 3.2 ± 1.4 for V_{EF}, and 5.2 ± 3.0 for Mo/U ratios), resulting in higher average values than in the lower part. Moreover, RSE EF profiles exhibit similar stratigraphic trends to the Fe_{py}/Fe_{HR} ratios in the upper part of the section, with progressively increasing RSE EFs after a two-step decrease, eventually remaining at the higher levels (Fig. 3).

Similar to the HSZ Fm., all samples in the XML Fm. have low to moderate Mo concentrations (mean 16.2 ± 16.2 ppm), with the exception of a markedly high value of 79.4 ppm. On the other hand, all investigated samples show moderate to strong RSE enrichments relative to UCC, with Mo_{EF}, U_{EF}, V_{EF} and Mo/U ratios ranging from 2.7 to 79.8, from 1.5 to 5.7, from 1.8 to 6.2, and from 1.5 to 14.1, respectively (Table S1). Stratigraphic trends in Mo_{EF}, U_{EF}, V_{EF} and Mo/U ratios are similar, and are characterized by high but variable RSE EFs in the lower part of the section, and moderate but uniform RSE EFs in the upper part of the section (Fig. 3).

4.3 C-N abundances and $\delta^{15}N$ values

The HSZ dolomites have low TOC concentrations (less than 1 wt%), with an average of 0.69 ± 1.54 wt%, whereas the HSZ shales have higher TOC contents of up to 7.59 wt%, with an average of 3.85 ± 1.80 wt% (Table S1). The TN profile exhibits a similar stratigraphic trend as TOC, in which TN contents are mostly around 0.04 ± 0.05 wt% in the HSZ dolomites and increase to an average of 0.13 ± 0.03 wt% towards the HSZ shales. Molar C/N ratios are higher than the Redfield value throughout most of the HSZ Fm. (average 32.29 versus 6.63) and fall within the typical range for Mesoproterozoic strata (Wang et al., 2020b). The $\delta^{15}N$ profile exhibits exclusively positive values (mean $+3.1 \pm 0.8$‰) and remains roughly invariant throughout the entire section, with most values falling within a narrow range between +2.7 to +4.1‰ (Fig. 4).

Similar to the high-TOC HSZ shales, the TOC content of XML shales is high, with maximum and average values of 5.85 wt% and 3.10 ± 1.42 wt%, respectively (Table S1). Stratigraphically, TOC contents in the XML shales show a slightly decreasing trend up-section, which is accompanied by relatively stable TN contents of 0.13 ± 0.02 wt%.

Molar C/N ratios exhibit a coupled pattern of secular variation with TOC content, with $C/N_{(mol)}$ declining from 46.49 to 17.75 upwards. $\delta^{15}N$ values consistently remain above +1‰, with an average of +3.1 ± 0.8‰ (Fig. 4). Similar to the HSZ Fm., the $\delta^{15}N$ values in the XML Fm. show an overall stability throughout the entire section.

5. Discussion

5.1 Water Column Redox Conditions

Fe speciation has been widely used as a proxy for ocean redox reconstruction based on extensive calibration in modern and ancient sediments, whereby Fe_{HR}/Fe_T > 0.38 is generally considered to provide a robust indication of anoxic bottom waters, Fe_{HR}/Fe_T < 0.22 commonly suggests oxic depositional conditions, while Fe_{HR}/Fe_T between 0.22 and 0.38 is equivocal and requires further investigation (Raiswell and Canfield,1998; Poulton and Raiswell, 2002; Poulton et al., 2010; Poulton and Canfield, 2011). Fe_{py}/Fe_{HR} ratios can be used to further differentiate between anoxic ferruginous (Fe_{py}/Fe_{HR} < 0.7) or euxinic (Fe_{py}/Fe_{HR} > 0.7–0.8) conditions (Poulton et al., 2004; Poulton and Canfield, 2011; Sperling et al., 2015; Raiswell et al., 2018). In the HSZ Fm., all samples have Fe_{HR}/Fe_T ratios greater than 0.38, suggesting persistent anoxic conditions. Fe_{py} dominates the Fe_{HR} pool with moderate to high Fe_{py}/Fe_{HR} ratios scattering close to 0.7, suggesting dominantly ferruginous to euxinic conditions. Fe speciation data of the XML Fm. resemble those of the HSZ. Fm., with generally high Fe_{HR}/Fe_T ratios (except for one sample with lower Fe_{HR}/Fe_T of 0.30) and moderate to high Fe_{py}/Fe_{HR} ratios close to 0.7, reflecting ferruginous to euxinic depositional conditions.

RSE EFs and their ratios can provide additional insight into local water column redox conditions, which is particularly useful when Fe speciation data fall within the equivocal range. Generally, RSE tend to be less soluble and more particle reactive under anoxic conditions than oxic conditions, leading to authigenic enrichments under locally anoxic conditions, provided that the global ocean is sufficiently oxic to host a large RSE reservoir (Tribovillard et al., 2006). The scavenging of Mo from seawater to sediments generally requires the presence of free H_2S in the water column (Algeo and Tribovillard, 2009), whereas effective drawdown of U and V tends to occur under anoxic conditions without the requirement for free H_2S (Anderson et al., 1989; Algeo and Tribovillard, 2009). Therefore, more pronounced enrichments in Mo relative to U and/or V support deposition under euxinic water column conditions (Algeo and Tribovillard, 2009). In the HSZ Fm., RSE EF profiles display generally moderate to high enrichments, coupled with elevated Mo/U ratios (Fig.3), which are broadly consistent with dominantly ferruginous to euxinic depositional conditions as identified by Fe speciation data. Despite the fluctuations, the overall elevated RSE enrichments and higher Mo/U ratios up-section likely indicate more effective removal of RSE under increasingly reducing (euxinic) conditions.

Similarly, in the XML Fm., RSE EF profiles exhibit co-enrichments in Mo, U and V, and correspondingly moderate to high Mo/U ratios, supporting our interpretation of

redox fluctuation between ferruginous and euxinic conditions. Although Fe speciation and RSE enrichment patterns provide evidence for euxinic conditions, moderate Mo concentrations in both studied sections (Fig.3) are lower than the empirical values from modern euxinic marine sediments (Algeo and Lyons, 2006; Scott and Lyons, 2012). However, given the evidently low Mo reservoir in Mesoproterozoic oceans (Scott et al., 2008; Partin et al., 2013), these signals are likely to reflect at least weakly euxinic depositional conditions. Our redox interpretation is consistent with the proposed global redox landscape during the Mesoproterozoic, supporting persistent anoxic and ferruginous deeper water conditions, with locally developed euxinia along some productive continental margins (Scott et al., 2008; Planavsky et al., 2011; Poulton and Canfield, 2011; Doyle et al., 2018; Chen et al., 2020).

5.2 Preservation of primary nitrogen isotopic signatures

Some synsedimentary and post-depositional processes, such as terrestrial input, burial diagenesis and/or metamorphism, can significantly modify primary $\delta^{15}N$ signatures (reviewed by Ader et al., 2016; Stüeken et al., 2016). Hence, it is necessary to evaluate whether $\delta^{15}N$ values in sedimentary rocks preserve the primary marine nitrogen isotope signals before making reliable biogeochemical interpretations.

Sedimentary nitrogen mainly exists in organic-bound nitrogen and inorganic clay-bound NH_4^+, and the latter mostly derives from *in situ* organic matter remineralization and is subsequently incorporated into the clay mineral lattice during diagenesis (Stüeken et al., 2017). This fraction of NH_4^+ generally preserves primary organic nitrogen isotope signals without isotopic fractionation (Ader et al., 2016; Koehler et al., 2017). In our samples, the positive correlation between TN and TOC contents indicates that the sedimentary nitrogen was mainly sourced from primary organic matter (Fig. 5A). We note that Fig 5A produces a positive TN intercept, meaning that the samples contain a small excess of nitrogen relative to organic matter. This excess can be derived from three possible sources: (1) infiltration of ammonium-rich fluids; (2) terrestrial input of N-rich clays; and (3) in-situ removal of organic carbon relative to nitrogen during diagenesis (Chen et al., 2019; Koehler et al., 2019). The first option is unlikely, because both the HSZ and the XML formations have relatively higher TOC contents than adjacent strata, arguing against the infiltration of N-bearing fluids from adjacent organic-rich layers. Regarding the second option, the input of allochthonous nitrogen bound to clay minerals would decrease C/N ratios and likely reset primary nitrogen isotope compositions. However, the lack of correlation between $\delta^{15}N$ values and C/N ratios (Fig. 5D) suggests that this scenario is unlikely. Hence, the positive TN-intercepts in the two studied sections are most likely attributed to the in-situ conversion of organic matter. For example, microbial sulfate reduction or methanogenesis are able to convert organic carbon to CO_2 and CH_4, respectively, while organic amines are left behind as ammonium. Under anoxic conditions, ammonium therefore typically accumulates in sediment pore waters (Rosenfeld, 1979).

The effect of burial diagenesis and metamorphism on primary $\delta^{15}N$ signatures has

been investigated in previous studies (e.g., Robinson et al., 2012; Stüeken et al., 2016). Isotopic fractionation associated with diagenetic alteration depends largely on water column redox conditions (Stüeken et al., 2016). Oxic diagenesis can result in positive nitrogen isotope shifts by up to 4‰ (Altabet et al., 1999; Freudenthal et al., 2001), while only a minor isotopic fractionation (< 1‰) is imparted during diagenesis under anoxic conditions (Altabet et al., 1999; Thunell et al., 2004). Given that both the HSZ Fm. and the XML Fm. were predominantly deposited under anoxic conditions, the effect of diagenetic alteration would have been limited. In terms of metamorphic alteration, the effect on $\delta^{15}N$ values is negligible (< 1‰) below greenschist facies, and minor (1 – 2‰) within the greenschist facies (reviewed by Ader et al., 2016; Stüeken et al., 2016). In the study area, rock pyrolysis and bitumen reflectance analyses (Zhang et al., 2020) suggest that both the HSZ and the XML formations have not experienced metamorphic temperatures above the oil window. This is consistent with the geochemical and mineralogical evidence from previous studies, suggesting that these rocks are well below greenschist facies (Luo et al., 2015; Shi et al., 2021). Furthermore, there is no correlation between $\delta^{15}N$ values and TOC, TN or C/N ratios (Fig. 5B–5D), suggesting that the effects of synsedimentary and post-depositional processes on primary $\delta^{15}N$ signatures, if any, are insignificant in our sample set. Thus, our $\delta^{15}N$ values can be used to reconstruct oceanic biogeochemical nitrogen cycling processes during the Mesoproterozoic.

5.3 A stable nitrate pool in Mesoproterozoic oceans

The primary source of bioavailable nitrogen in seawater is through biological nitrogen fixation, which reduces the inert atmospheric N_2 to bioavailable NH_4^+, with a small isotopic fractionation of –1‰ on average (range from –2‰ to +1‰), but fractionations can be as large as –4‰ under Fe^{2+}-rich or thermophilic conditions (Zerkle et al., 2008; Zhang et al., 2014). Alternative Fe- or V-based nitrogenases could induce larger isotopic fractionations of –6‰ to –8‰ (Zhang et al., 2014); however, such scenarios are very rare in the geological record (Stüeken et al., 2016). Under oxic conditions, NH_4^+ is generally quantitatively oxidized to NO_3^- via nitrification, with negligible isotopic fractionation (Sigman et al., 2009). Thus, NO_3^- rather than NH_4^+ serves as the dominant nitrogen species in the oxygenated photic zone, probably feeding the majority of primary producers. Partial assimilation could produce large isotopic fractionations of –5 to –10‰, but these fractionations are generally not expressed because assimilation is near quantitative in most modern and ancient oceans (Altabet and Francois, 1994).

Denitrification and anammox are the two major pathways of N loss from the ocean under suboxic/anoxic conditions. Both processes can impart large isotopic fractionations of –5 to –30‰ if they occur within the water column, but the net effects are negligible if they occur within sedimentary pore waters (Lam et al., 2009; Sigman et al., 2009; Lam and Kuypers, 2011). In the modern ocean, water-column denitrification and/or anammox occurring in oxygen-minimum zones are therefore responsible for pushing the marine nitrate pool to slightly positive values (e.g., +5‰ in

modern seawater; Tesdal et al., 2013). Uptake of this isotopically heavy nitrate into biomass thus preserves indirect evidence for a large nitrate reservoir in seawater that underwent partial denitrification/anammox in anoxic regions, but remained large enough to sustain a significant portion of the biosphere. If anoxic waters expand in volume, more nitrate is removed and the residual pool becomes further enriched in ^{15}N. Subsequently, marine systems produce different responses depending on the reservoir size of the residual nitrate pool. Considering that the fixation of N_2 gas into biomass is an energetically costly process, it is typically only performed in environments where fixed nitrogen is limiting (Koehler et al., 2017). Therefore, if the dwindling nitrate reservoir remains large enough to sustain a significant portion of the biosphere, biological N_2 fixation would not be induced and the δ^{15}N signal associated with incomplete water-column denitrification and/or anammox would be expressed. Otherwise, the dwindling nitrate reservoir would induce the onset of biological N_2 fixation, such that bulk sedimentary δ^{15}N values are pulled back towards lower values near 0‰ (Sigman et al., 2009; Kipp et al., 2018). Hence, different states of the biogeochemical nitrogen cycle have the potential to generate distinct δ^{15}N fingerprints in sediments, if alternative scenarios can be ruled out.

In the ~1460 Ma HSZ Fm. and ~1380 Ma XML Fm., stratigraphic profiles exhibit persistently positive δ^{15}N values (+3.1 ± 0.8‰) which are outside the typical range for nitrogen fixation (Fig. 4). Three alternative mechanisms have been invoked to explain such positive δ^{15}N values (> +2‰) in marine environments: (i) Partial assimilation of NH_4^+ preferentially uptakes the isotopically lighter isotope (^{14}N) and concomitantly drives the residual NH_4^+ pool to ^{15}N-enrichment (Papineau et al., 2009; Kipp et al., 2018). When this ^{15}N-enriched NH_4^+ pool is sequestered and quantitatively consumed by primary producers elsewhere in the basin, a positive δ^{15}N would be expected. However, this scenario seems unlikely since partial assimilation would result in two opposite isotopic facies. Neither our samples nor compiled δ^{15}N data capture very negative δ^{15}N values (lighter than –2‰) across the Yanliao basin, as one would expect for localities where NH_4^+ levels had been high enough to allow for partial assimilation into biomass (Fig. 6).

(ii) Partial nitrification of NH_4^+ followed by quantitative denitrification/anammox would remove ^{15}N-depleted NO_3^- from the system, leaving isotopically heavy NH_4^+ as the dominant dissolved nitrogen species for primary productivity (Thomazo et al., 2011). However, nitrification is generally prone to go to completion even at micromolar O_2 levels (Fuchsman et al., 2008; Fussel et al., 2012). Partial nitrification has only been documented in basins with frequent fluctuations in oxygen concentration, and cannot exist over long geological timescales because progressive loss of isotopically light ^{14}N would lead to an isotopic imbalance. This scenario lacks a sink for heavy N, in contrast to the modern ocean, where heavy N is lost through sedimentary denitrification. Moreover, this process would generate a large range in sedimentary δ^{15}N values (Granger et al., 2011; Morales et al., 2014), which is inconsistent with the uniformly positive δ^{15}N values recorded in our samples.

(iii) As in the modern ocean, incomplete denitrification and/or anammox transform isotopically lighter dissolved nitrogen into N_2O/N_2 gas, which escapes to the atmosphere, rendering the residual NO_3^- pool enriched in ^{15}N, which would subsequently be assimilated by organisms (Kuypers et al., 2003; Sigman et al., 2009). This scenario has been considered as the major mechanism to explain positive sedimentary $\delta^{15}N$ values in a number of modern and ancient sediments (Sigman et al., 2009; Stüeken, 2013; Tesdal et al., 2013; Koehler et al., 2017; Liu et al., 2020), and seems to be the most plausible cause for the positive $\delta^{15}N$ values in our samples. The exclusively positive $\delta^{15}N$ values in both studied sections are thus indirect evidence for a stable nitrate pool in oxic surface waters, with a relatively deep chemocline probably below the photic zone, such that denitrification did not diminish nitrate abundance (Kipp et al., 2018). This inference is consistent with a Mesoproterozoic redox-stratified ocean, with anoxic deeper waters overlain by shallower oxic waters (Scott et al., 2008; Planavsky et al., 2011; Poulton and Canfield, 2011; Doyle et al., 2018). If we combine our data with previously published nearshore $\delta^{15}N$ data for the Yanliao basin (Wang et al., 2020b), an onshore to offshore gradient is well expressed (Fig. 6). This is consistent with the trend observed in other Mesoproterozoic basins (Stüeken, 2013; Koehler et al., 2017), suggesting that a decrease in nitrate availability towards offshore environments may be a global feature of Mesoproterozoic oceans. However, unlike the Belt basin, offshore $\delta^{15}N$ values in the Yanliao, Bangemall and Roper basins are more positive than those derived from nitrogen fixation alone (Fig. 6). This difference may reflect the high degree of restriction in the Belt Basin and indicates that in other basins, nitrate availability decreased less severely. Nevertheless, these observations support the common development of a spatial gradient in nitrate bioavailability.

5.4 Implications for eukaryote evolution

Nitrogen is a bio-essential nutrient for all living organisms. Together with phosphorus, it is important for controlling cellular metabolism and ultimately shaping the long-term evolution of life (e.g., Tyrrell, 1999; Canfield et al., 2010). Both NH_4^+ and NO_3^- comprise biologically available nitrogen; however, they are not utilized in the same way due to their differing redox states. Eukaryotes are incapable of N_2 fixation and are usually outcompeted by prokaryotes in the assimilation of NH_4^+ (Anbar and Knoll, 2002 and references therein). Thus, waters depleted in fixed nitrogen would favor prokaryotes over eukaryotes. Conversely, nitrate-rich waters may not only meet the higher nutrient requirements of larger eukaryotic organisms, but perhaps also limit prokaryote abundances by grazing (Brocks et al., 2017; Reinhard et al., 2020), leading to a eukaryote-dominated ecosystems. It has been suggested that the development of locally stable nitrate pools in the Paleoproterozoic surface ocean may have promoted the proliferation of cyanobacteria and potentially the emergence of eukaryotes (e.g., Kipp et al., 2018; Miao et al., 2019), and a global increase in nutrient levels in late Neoproterozoic surface ocean may have further allowed for the rapid diversification of eukaryotes (Brocks et al., 2017; Wang et al., 2018; Chen et al., 2019). By contrast, the extensive loss of fixed N in response to the expansion of anoxic conditions in the Mesoproterozoic oceans was thought to have resulted in nutrient limitation, which in

turn protracted the diversification of eukaryotes at that time (Anbar and Knoll, 2002; Reinhard et al., 2013; Stüeken, 2013).

Our geochemical data from the Yanliao basin suggest that a stable and moderate nitrate pool may have been established in offshore seawater during the Mesoproterozoic (Fig. 6). In a broader context, a compilation of sedimentary $\delta^{15}N$ data (Table S2) from different Mesoproterozoic basins worldwide (Fig. 7) displays a persistent aerobic $\delta^{15}N$ signature, giving further support that nitrate limitation may have been less severe in the Mesoproterozoic oceans than previously considered. Nevertheless, although a stable nitrate pool may have built up in Mesoproterozoic oceans, sedimentary $\delta^{15}N$ values remain largely ^{15}N-depleted compared to modern marine sediments (~ +5‰ on average; e.g., Tesdal et al., 2013), indicating that the size of the nitrate pool in Mesoproterozoic oceans was significantly smaller than in eukaryote-dominated modern oceans. The moderate nitrate-rich seawater may have been sufficient to sustain a small population of eukaryotic organisms in Mesoproterozoic oceans.

This proposition is consistent with previously published paleontological studies and biomarker records (e.g., Buick and Knoll, 1999; Javaux et al., 2001; Dutkiewicz et al., 2003; Brocks et al., 2005; Miao et al., 2021; Zhang et al., 2021). The generally moderate nitrate pool in Mesoproterozoic oceans inferred from $\delta^{15}N$ data coincides with the presence of eukaryotic microfossils and a low abundance of eukaryotic biomarkers (Fig. 7), suggesting that eukaryotic organisms at least contribute partially to total primary productivity in Mesoproterozoic marine ecosystem. Locally nitrate-rich waters may have been necessary to trigger eukaryotic diversification and the rise of eukaryotes to ecological dominance. This is supported by the highly positive $\delta^{15}N$ values (7.47 ± 1.53‰) recorded in the ~1.56 Ga Gaoyuzhuang Fm., North China (Wang et al., 2020b), which coincides with the appearance of decimetre-scale, multicellular eukaryotes (Zhu et al., 2016). Similarly, an onshore to offshore nitrate gradient in the ~1.5 Ga Bangemall basin and the ~1.4–1.5 Ga Roper basin (Koehler et al., 2017) corresponds well to a trend of decreasing diversity and abundance in eukaryotic microfossils (Buick and Knoll, 1999; Javaux et al., 2001), suggesting a close linkage between oceanic nitrate availability and eukaryotic diversity. Although the moderate nitrate-rich Mesoproterozoic seawater was likely insufficient to trigger evolutionary innovation, it may have played a role in the ability of eukaryotes to persist in generally inhospitable Mesoproterozoic oceans until a more favorable environment emerged in the Neoproterozoic.

Conclusions

In this study, we present a multi-proxy geochemical dataset for two new drill-core sections from the ~1460 Ma HSZ Fm. and ~1380 Ma XML Fm., North China. Fe speciation combined with Mo concentrations and RSE EFs indicate that both formations were deposited under frequently fluctuating redox conditions between ferruginous and weakly euxinic. Our new data support a stratified Mesoproterozoic

ocean in which anoxic deeper waters were overlain by oxic surface waters, with euxinia dynamically developed along some productive continental margins. Although deeper offshore waters remained largely anoxic, a stable nitrate pool likely developed within the photic zone, as suggested by uniformly positive $\delta^{15}N$ (+3.1 ± 0.8‰) values. These values are interpreted as indirect evidence of aerobic nitrogen cycling, dominated by efficient nitrification of ammonium in the surface ocean and incomplete denitrification and/or anammox at the oxic/anoxic interface in the water column. The aerobic $\delta^{15}N$ signatures presented in a compilation of the global Mesoproterozoic sedimentary $\delta^{15}N$ record suggest that oceanic nitrate levels may not have been as limited as previously considered. However, as previously shown, the $\delta^{15}N$ data indicate an onshore-to-offshore decrease in nitrate availability. The overall size of the nitrate pool was apparently smaller than that of eukaryote-dominated modern oceans. The moderate nitrate levels in the Mesoproterozoic oceans coincide with the presence of eukaryotic microfossils and a low abundance of eukaryotic biomarkers, suggesting that this moderate nitrate availability may have been sufficient to sustain a small population of eukaryotic organisms in Mesoproterozoic marine ecosystems.

Declaration of Competing Interest

The authors declare that they have no known competing financial interests or personal relationships that could have appeared to influence the work reported in this paper.

Acknowledgments

Appendix A. Supplementary data

References

- Ader, M., Thomazo, C., Sansjofre, P., Busigny, V., Papineau, D., Laffont, R., Cartigny, P., Halverson, G.P., 2016. Interpretation of the nitrogen isotopic composition of Precambrian sedimentary rocks: assumptions and perspectives. Chem. Geol. 429, 93–110.
- Alcott, L.J., Krause, A.J., Hammarlund, E.U., Bjerrum, C.J., Scholz, F., Xiong, Y., Hobson, A.J., Neve, L., Mills, B.J., März, C., Schnetger, B., Bekker, A., Poulton, S.W., 2020. Development of iron speciation reference materials for palaeoredox analysis. Geostandards and Geoanalytical Research, 44, 581–1591.
- Algeo, T.J., Lyons, T.W., 2006. Mo-total organic carbon variation in modern anoxic

environments: Implications for analysis of paleoredox and paleohydrographic conditions. Paleoceanography 21, 1–23.

- Algeo, T.J., Tribovillard, N., 2009. Environmental analysis of paleoceanographic systems based on molybdenum-uranium covariation. Chem. Geol. 268, 211–225.
- Altabet, M.A., Francois, R., 1994. Sedimentary nitrogen isotopic ratio as a recorder for 1200 surface ocean nitrate utilization. Global Biogeochem. Cycles 8, 103–116.
- Altabet, M.A., Pilskaln, C., Thunell, R., Pride, C., Sigman, D., Chavez, F., Francois, R., 1999. The nitrogen isotope biogeochemistry of sinking particles from the margin of the Eastern North Pacific. Deep Sea Res. Part I: Oceanogr. Res. Pap. 46, 655–679.
- Anbar, A.D., Knoll, A.H., 2002. Proterozoic ocean chemistry and evolution: a bioinorganic bridge? Science 297, 1137–1142.
- Anderson, R.F., Fleisher, M.Q., LeHuray, A.P., 1989. Concentration, oxidation state, and particulate flux of uranium in the Black Sea. Geochem. Cosmochim. Acta 53, 2215–2224.
- Brasier, M.D., Lindsay, J.F., 1998. A billion years of environmental stability and the emergence of eukaryotes: new data from northern Australia. Geology 26, 555–558.
- Brocks, J.J., Jarrett, A.J.M., Sirantoine, E., Hallmann, C., Hoshino, Y., Liyanage, T., 2017. The rise of algae in Cryogenian oceans and the emergence of animals. Nature 548 (7669), 578–581.
- Brocks, J.J., Love, G.D., Summons, R.E., Knoll, A.H., Logan, G.A., Bowden, S.A., 2005. Biomarker evidence for green and purple sulphur bacteria in a stratified Palaeoproterozoic sea. Nature 437, 866–870.
- Buick, R., Knoll, A.H., 1999. Acritarchs and microfossils from the Mesoproterozoic Bangemall Group, Northwestern Australia. J. Paleontol. 73, 744–764.
- Canfield, D.E., Glazer, A.N., Falkowski, P.G., 2010. The Evolution and Future of Earth's Nitrogen Cycle. Science 330, 192–196.
- Canfield, D.E., Raiswell, R., Westrich, J.T., Reaves, C.M., Berner, R.A., 1986. The use of chromium reduction in the analysis of reduced inorganic sulfur in sediments and shales. Chem. Geol. 54, 149–155.
- Canfield, D.E., Zhang, S.C., Frank, A.B., Wang, X.M., Wang, H.J., Su, J., Ye, Y.T., Frei, R., 2018. Highly fractionated chromium isotopes in Mesoproterozoic-aged shales and atmospheric oxygen. Nat. Commun. 9, 2871.
- Chen, X.Y., Li, M.H., Sperling, E.A., Zhang, T.G., Zong, K.Q., Liu, Y.S., Shen, Y., 2020. Mesoproterozoic paleo-redox changes during 1500–1400 Ma in the Yanshan Basin, North China. Precambrian Res. 347, 105835.
- Chen, Y., Diamond, C.W., Stüeken, E.E., Cai, C.F., Gill, B.C., Zhang, F.F., Bates, S.M., Chu, X.L., Ding, Y., Lyons, T.W., 2019. Coupled evolution of nitrogen cycling and redoxcline dynamics on the Yangtze Block across the Ediacaran-Cambrian transition. Geochim. Cosmochim. Acta 257, 243–265.
- Cheng, D.W., Zhang, S.C., Zhang, Z.J., Zhou, C.M., Wang, H.J., Yuan, X.J., Chen, X.Y., 2020. An astronomically calibrated stratigraphy of the Mesoproterozoic Hongshuizhuang Formation, North China: Implications for pre-Phanerozoic changes in Milankovitch orbital parameters. J. Asian Earth Sci. 199, 104408.
- Clarkson, M.O., Poulton, S.W., Guilbaud, R., Wood, R.A., 2014. Assessing the utility of

Fe/Al and Fe-speciation to record water column redox conditions in carbonate-rich sediments. Chem. Geol. 382, 111–122.

- Cole, D.B., Reinhard, C.T., Wang, X., Gueguen, B., Halverson, G.P., Gibson, T., Hodgskiss, M.S.W., McKenzie, N.R., Lyons, T.W., Planavsky, N.J., 2016. A shale-hosted Cr isotope record of low atmospheric oxygen during the Proterozoic. Geology 44, 555–558.
- Doyle, K.A., Poulton, S.W., Newton, R.J., Podkovyrov, V.N., Bekker, A., 2018. Shallow water anoxia in the Mesoproterozoic ocean: evidence from the Bashkir Meganticlinorium, Southern Urals. Precambrian Res. 317, 196–210.
- Du, Y., Song, H.Y., Tong, J.N., Algeo, T.J., Li, Z., Song, H.J., Huang, J.D., 2021. Changes in productivity associated with algal-microbial shifts during the Early Triassic recovery of marine ecosystems. Geol. Soc. Am. Bull. 133(1–2), 362–378.
- Dutkiewicz, A., Volk, H., Ridley, J., George, S., 2003. Biomarkers, brines, and oil in the Mesoproterozoic, Roper Superbasin, Australia. Geology 31, 981–984.
- Fairchild, T.R., Schopf, J.W., Shen-Miller, J., Guimarães, E.M., Edwards, M.D., Lagstein, A., Li, X., Pabst, M., de Melo-Filho, L.S., 1996. Recent discoveries of Proterozoic microfossils in south-central Brazil. Precambrian Res. 80, 125–152.
- Freudenthal, T., Wagner, T., Wenzhöfer, F., Zabel, M., Wefer, G., 2001. Early diagenesis of organic matter from sediments of the eastern subtropical Atlantic: evidence from stable nitrogen and carbon isotopes. Geochim. Cosmochim. Acta 65, 1795–1808.
- Fuchsman, C.A., Murray, J.W., Konovalov, S.K., 2008. Concentration and natural stable isotope profiles of nitrogen species in the Black Sea. Mar. Chem. 111, 90–105.
- Fussel, J., Lam, P., Lavik, G., Jensen, M.M., Holtappels, M., Gunter, M., Kuypers, M.M., 2012. Nitrite oxidation in the Namibian oxygen minimum zone. ISME J. 6, 1200–1209.
- Gilleaudeau, G.J., Frei, R., Kaufman, A.J., Kah, L.C., Azmy, K., Bartley, J.K., Chernyavskiy, P., Knoll, A.H., 2016. Oxygenation of the mid-Proterozoic atmosphere: clues from chromium isotopes in carbonates. Geochem. Perspect. Lett. 2, 178–187.
- Gilleaudeau, G.J., Sahoo, S.K., Ostrander, C.M., Owens, J.D., Poulton, S.W., Lyons, T.W., Anbar, A.D., 2020. Molybdenum isotope and trace metal signals in an iron-rich Mesoproterozoic ocean: a snapshot from the Vindhyan Basin. India. Precambrian Res. 343, 105718.
- Granger, J., Prokopenko, M.G., Sigman, D.M., Mordy, C.W., Morse, Z.M., Morales, L.V., Sambrotto, R.N., Plessen, B., 2011. Coupled nitrification–denitrification in sediment of the eastern Bering Sea shelf leads to (15)N enrichment of fixed N in shelf waters. J. Geophys. Res. Oceans 116, C11006(1–18).
- Hodgskiss, M.S.W., Sansjofre, P., Kunzmann, M., Sperling, E.A., Cole, D.B., Crockford, P.W., Gibson, T.M., Halverson, G.P., 2020. A high-TOC shale in a low productivity world: The late Mesoproterozoic Arctic Bay Formation, Nunavut. Earth Planet. Sci. Lett. 544, 116384.
- Holland, H.D., 2006. The oxygenation of the atmosphere and oceans. Philos. Trans. Roy. Soc. B 361, 903–915.
- Javaux, E.J., Knoll, A.H., Walter, M.R., 2001. Morphological and ecological complexity in early eukaryotic ecosystems. Nature 412, 66–69.
- Kipp, M.A., Stüeken, E.E., Yun, M., Bekker, A., Buick, R., 2018. Pervasive aerobic

nitrogen cycling in the surface ocean across the Paleoproterozoic Era. Earth Planet. Sci. Lett. 500, 117–126.

- Koehler, M.C., Stüeken, E.E., Hillier, S., Prave, A.R., 2019. Limitation of fixed nitrogen and deepening of the carbonate-compensation depth through the Hirnantian at Dob's Linn, Scotland. Palaeogeogr. Palaeoclimatol. Palaeoecol. 534, 1–15.

- Koehler, M.C., Stüeken, E.E., Kipp, M.A., Buick, R., Knoll, A.H., 2017. Spatial and temporal trends in Precambrian nitrogen cycling: A Mesoproterozoic offshore nitrate minimum. Geochim. Cosmochim. Acta 198, 315–337.

- Kuypers, M.M.M., Sliekers, A.O., Lavik, G., Schmid, M., Jørgensen, B.B., Kuenen, J.G., Sinninghe Damsté, J.S., Strous, M., Jetten, M.S., 2003. Anaerobic ammonium oxidation by anammox bacteria in the Black Sea. Nature 422, 608.

- Lam, P., Kuypers, M.M.M., 2011. Microbial nitrogen cycling processes in oxygen minimum zones. Mar. Sci. Ann. Rev. 3, 317–345.

- Lam, P., Lavik, G., Jensen, M.M., van de Vossenberg, J., Schmid, M., Woebken, D., Gutiérrez, D., Amann, R., Jetten, M.S.M., Kuypers, M.M.M., 2009. Revising the nitrogen cycle in the Peruvian oxygen minimum zone. Proc. Natl. Acad. Sci. U.S.A. 106, 4752–4757.

- Li, H.K., Lu, S.N., Su, W.B., Xiang, Z.Q., Zhou, H.Y., Zhang, Y.Q., 2013. Recent advances in the study of the Mesoproterozoic geochronology in the North China Craton. J. Asian Earth Sci. 72, 216–227.

- Li, H.K., Su, W.B., Zhou, H.Y., Xiang, Z.Q., Tian, H., Yang, L.G., Huff, W.D., Ettensohn, F.R., 2014. The first precise age constraints on the Jixian system of the Meso- to Neoproterozoic standard section of China: SHRIMP zircon U-Pb dating of bentonites from the Wumishan and Tieling formations in the Jixian Section, North China Craton. Acta Petrol. Sin. 30, 2999–3012 (in Chinese with English abstract).

- Liu, Y., Magnall, J.M., Gleeson, S.A., Bowyer, F., Poulton, S.W., Zhang, J.C., 2020. Spatio-temporal evolution of ocean redox and nitrogen cycling in the early Cambrian Yangtze Ocean. Chem. Geol. 554, 119803.

- Luo, G.M., Hallmann, C., Xie, S.C., Ruan, X.Y., Summons, R.E., 2015. Comparative microbial diversity and redox environments of black shale and stromatolite facies in the Mesoproterozoic Xiamaling Formation. Geochim. Cosmochim. Acta 151, 150–167.

- Luo, G.M., Junium, C.K., Kump, L.R., Huang, J.H., Li, C., Feng, Q.L., Shi, X.Y., Bai, X., Xie, S.C., 2014. Shallow stratification prevailed for ~1700 to ~1300 Ma ocean: evidence from organic carbon isotopes in the North China Craton. Earth Planet. Sci. Lett. 400, 219–232.

- Luo, J., Long, X.P., Bowyer, F.T., Mills, B.J.W., Li, J., Xiong, Y.J., Zhu, X.K., Zhang, K., Poulton, S.W., 2021. Pulsed oxygenation events drove progressive oxygenation of the early Mesoproterozoic ocean. Earth Planet. Sci. Lett. 559, 116754.

- Lyons, T.W., Reinhard, C.T., Planavsky, N.J., 2014. The rise of oxygen in Earth's early ocean and atmosphere. Nature 506(7488), 307–315.

- Ma, K., Hu, S.Y., Wang, T.S., Zhang, B.M., Qin, S.F., Shi, S.Y., Wang, K., Huang, Q.Y., 2017. Sedimentary environments and mechanisms of organic matter enrichment in the Mesoproterozoic Hongshuizhuang Formation of northern China. Palaeogeogr. Palaeoclimatol. Palaeoecol. 475, 176–187.

- McLennan, S.M., 2001. Relationships between the trace element composition of sedimentary rocks and upper continental crust. Geochem. Geophys. Geosyst. 2, 203–236.
- Miao, L.Y., Moczydłowska, M., Zhu, M.Y., 2021. A diverse organic-walled microfossil assemblage from the Mesoproterozoic Xiamaling Formation, North China. Precambrian Res. 360, 106235.
- Miao, L.Y., Moczydłowska, M., Zhu, S.X., Zhu, M.Y., 2019. New record of organic-walled, morphologically distinct microfossils from the late Paleoproterozoic Changcheng Group in the Yanshan Range, North China. Precambrian Res. 321, 172–198.
- Morales, L.V., Granger, J., Chang, B.X., Prokopenko, M.G., Plessen, B., Gradinger, R., Sigman, D.M., 2014. Elevated $^{15}N/^{14}N$ in particulate organic matter, zooplankton, and diatom frustule-bound nitrogen in the ice-covered water column of the Bering Sea eastern shelf. Deep Sea Res. Part II Topical Stud. Oceanogr. 109, 100–111.
- Ossa Ossa, F.O., Eickmann, B., Hofmann, A., Planavsky, N.J., Asael, D., Pambo, F., Bekker, A., 2018. Two-step deoxygenation at the end of the Paleoproterozoic Lomagundi Event. Earth Planet. Sci. Lett. 486, 70–83.
- Otero-Ferrer, J.L., Cermeño, P., Bode, A., Fernández-Castro, B., Gasol, J.M., Morán, X.A.G., Marañon, E., Moreira-Coello, V., Varela, M.M., Villamaña, M., Mouriño-Carballido, B., 2018. Factors controlling the community structure of picoplankton in contrasting marine environments. Biogeosciences 15, 6199–6220.
- Papineau, D., Purohit, R., Goldberg, T., Pi, D., Shields, G.A., Bhu, H., Steele, A., Fogel, M.L., 2009. High primary productivity and nitrogen cycling after the Paleoproterozoic phosphogenic event in the Aravalli supergroup, India. Precambrian Res. 171, 37–56.
- Partin, C.A., Bekker, A., Planavsky, N.J., Scott, C.T., Gill, B.C., Li, C., Podkovyrov, V., Maslov, A., Konhauser, K.O., Lalonde, S.V., Love, G.D., Poulton, S.W., Lyons, T.W., 2013. Large-scale fluctuations in Precambrian atmospheric and oceanic oxygen levels from the record of U in shales. Earth Planet. Sci. Lett. 369, 284–293.
- Planavsky, N.J., McGoldrick, P., Scott, C.T., Li, C., Reinhard, C.T., Kelly, A.E., Chu, X., Bekker, A., Love, G.D., Lyons, T.W., 2011. Widespread iron-rich conditions in the mid-Proterozoic ocean. Nature 477, 448–451.
- Planavsky, N.J., Reinhard, C.T., Wang, X.L., Thomson, D., McGoldrick, P., Rainbird, R.H., Johnson, T., Fischer, W.W., Lyons, T.W., 2014. Low Mid-Proterozoic atmospheric oxygen levels and the delayed rise of animals. Science 346, 635–638.
- Poulton, S.W., Canfield, D.E., 2005. Development of a sequential extraction procedure for iron: implications for iron partitioning in continentally derived particulates. Chem. Geol. 214, 209–221.
- Poulton, S.W., Canfield, D.E., 2011. Ferruginous conditions: a dominant feature of the ocean through Earth's history. Elements 7, 107–112.
- Poulton, S.W., Fralick, P.W., Canfield, D.E., 2004. The transition to a sulphidic ocean ~1.84 billion years ago. Nature 431, 173–177.
- Poulton, S.W., Fralick, P.W., Canfield, D.E., 2010. Spatial variability in oceanic redox structure 1.8 billion years ago. Nat. Geosci. 3, 486–490.
- Poulton, S.W., Raiswell, R., 2002. The low-temperature geochemical cycle of iron: from

continental fluxes to marine sediment deposition. Am. J. Sci. 302, 774–805.

- Raiswell, R., Canfield, D.E., 1998. Sources of iron for pyrite formation in marine sediments. Am. J. Sci. 298, 219–245.
- Raiswell, R., Hardisty, D.S., Lyons, T.W., Canfield, D.E., Reinhard, C.T., 2018. The iron paleoredox proxies: a guide to the pitfalls, problems and proper practice. Am. J. Sci. 318, 491–526.
- Redfield, A.C., 1934. On the Proportions of Organic Derivatives in Sea Water and Their Relation to the Composition of Plankton. James Johnstone Memorial Volume. University press of Liverpool, pp. 176–192.
- Reinhard, C.T., Planavsky, N.J., Gill, B.C., Ozaki, K., Robbins, L.J., Lyons, T.W., Fischer, W.W., Wang, C.J., Cole, D.B., Konhauser, K.O., 2017. Evolution of the global phosphorus cycle. Nature 541, 386–389.
- Reinhard, C.T., Planavsky, N.J., Olson, S.L., Lyons, T.W., Erwin, D.H., 2016. Earth's oxygen cycle and the evolution of animal life. Proc. Natl. Acad. Sci. U.S.A. 113, 8933–8938.
- Reinhard, C.T., Planavsky, N.J., Robbins, L.J., Partin, C.A., Gill, B.C., Lalonde, S.V., Bekker, A., Konhauser, K.O., Lyons, T.W., 2013. Proterozoic ocean redox and biogeochemical stasis. Proc. Natl. Acad. Sci. U.S.A. 110, 5357–5362.
- Reinhard, C.T., Planavsky, N.J., Ward, B.A., Love, G.D., Le Hir, G., Ridgwell, A., 2020. The impact of marine nutrient abundance on early eukaryotic ecosystems. Geobiology 18 (2), 139–151.
- Robinson, R.S., Kienast, M., Albuquerque, A.L., Altabet, M., Contreras, S., Holz, R.D., Dubois, N., Francois, R., Galbraith, E., Hsu, T.C., Ivanochko, T., Jaccard, S., Kao, S.J., Kiefer, T., Kienast, S., Lehmann, M.F., Martinez, P., McCarthy, M., Mobius, J., Pedersen, T., Quan, T.M., Ryabenko, E., Schmittner, A., Schneider, R., Schneider-Mor, A., Shigemitsu, M., Sinclair, D., Somes, C., Studer, A., Thunell, R., Yang, J.Y., 2012. A review of nitrogen isotopic alteration in marine sediments. Paleoceanography 27, PA4203.
- Rosenfeld, J.K., 1979. Ammonium adsorption in nearshore anoxic sediments 1. Limnology and Oceanography, 24(2), 356-364.
- Scott, C., Lyons, T.W., 2012. Contrasting molybdenum cycling and isotopic properties in euxinic versus non-euxinic sediments and sedimentary rocks: Refining the paleoproxies. Chem. Geol. 324–325, 19–27.
- Scott, C., Lyons, T.W., Bekker, A., Shen, Y., Poulton, S.W., Chu, X., Anbar, A.D., 2008. Tracing the stepwise oxygenation of the Proterozoic ocean. Nature 452, 456–459.
- Shang, M.H., Tang, D.J., Shi, X.Y., Zhou, L.M., Zhou, X.Q., Song, H.Y., Jiang, G.Q., 2019. A pulse of oxygen increase in the early Mesoproterozoic Ocean at ca. 1.57–1.56 Ga. Earth Planet. Sci. Lett. 527, 115797.
- Sheen, A.I., Kendall, B., Reinhard, C.T., Creaser, R.A., Lyons, T.W., Bekker, A., Poulton, S.W., Anbar, A.D., 2018. A model for the oceanic mass balance of rhenium and implications for the extent of Proterozoic ocean anoxia. Geochim. Cosmochim. Acta 227, 75–95.
- Shi, Q., Shi, X.Y, Tang, D.J., Fan, C.H., Wei, B.L., Li, Yang., 2021. Heterogeneous oxygenation coupled with low phosphorus bio-availability delayed eukaryotic

diversification in Mesoproterozoic oceans: Evidence from the ca 1.46 Ga Hongshuizhuang Formation of North China. Precambrian Res. 354, 106050.

- Sigman, D.M., Karsh, K.L., Casciotti, K.L., 2009. Nitrogen isotopes in the ocean. In: Steele, J.H., Thorpe, S.A., Turekian, K.K. (Eds.), Encyclopedia of Ocean Sciences. Academic Press, Oxford, pp. 40–54.
- Sperling, E.A., Rooney, A.D., Hays, L., Sergeev, V.N., Vorob'Eva, N.G., Sergeeva, N.D., Selby, D., Johnston, D.T., Knoll, A.H., 2014. Redox heterogeneity of subsurface waters in the Mesoproterozoic ocean. Geobiology 12, 373–386.
- Sperling, E.A., Wolock, C.J., Morgan, A.S., Gill, B.C., Marcus, K., Halverson, G.P., Macdonald, F.A., Knoll, A.H., Johnston, D.T., 2015. Statistical analysis of iron geochemical data suggests limited late Proterozoic oxygenation. Nature 523, 451–454.
- Stüeken, E.E., 2013. A test of the nitrogen-limitation hypothesis for retarded eukaryote radiation: nitrogen isotopes across a Mesoproterozoic basinal profile. Geochim. Cosmochim. Acta 120, 121–139.
- Stüeken, E.E., Kipp, M.A., Koehler, M.C., Buick, R., 2016. The evolution of Earth's biogeochemical nitrogen cycle. Earth-Sci. Rev. 160, 220–239.
- Stüeken, E.E., Viehmann, S., Hohl, S.V., 2021. Contrasting nutrient availability between marine and brackish waters in the late Mesoproterozoic: Evidence from the Paranoá Group, Brazil. Geobiology 1472–4677.
- Stüeken, E.E., Zaloumis, J., Meixnerová, J., Buick, R., 2017. Differential metamorphic effects on nitrogen isotopes in kerogen extracts and bulk rocks. Geochim. Cosmochim. Acta 217, 80–94.
- Su, W.B., Li, H.K., Huff, W.D., Ettensohn, F.R., Zhang, S.H., Zhou, H.Y., Wan, Y.S., 2010. SHRIMP U-Pb dating for a K-bentonite bed in the Tieling Formation, North China. Sci. Bull. 55(29), 3312–3323.
- Tesdal, J.E., Galbraith, E.D., Kienast, M., 2013. Nitrogen isotopes in bulk marine sediment: Linking seafloor observations with subseafloor records. Biogeosciences 10, 101–118.
- Thomazo, C., Ader, M., Phillippot, P., 2011. Extreme ^{15}N enrichment in 2.72-Gyr-old sediments: evidence for a turning point in the nitrogen cycle. Geobiology 9, 107–120.
- Thunell, R.C., Sigman, D.M., Muller-Karger, F., Astor, Y., Varela, R., 2004. Nitrogen isotope dynamics of the cariaco basin, Venezuela. Glob. Biogeochem. Cycles 18, GB3001.
- Tribovillard, N., Algeo, T.J., Lyons, T., Riboulleau, A., 2006. Trace metals as paleoredox and paleoproductivity proxies: an update. Chem. Geol. 232, 12–32.
- Tyrrell, T., 1999. The relative influences of nitrogen and phosphorus on oceanic primary production. Nature 400, 525–531.
- Wang, H.Y., Zhang, Z.H., Li, C., Algeo, T.J., Cheng, M., Wang, W., 2020a. Spatio-temporal redox heterogeneity and transient marine shelf oxygenation in the Mesoproterozoic ocean. Geochim. Cosmochim. Acta 270, 201–217.
- Wang, X.M., Zhang, S.C., Wang, H.J., Bjerrum, C.J., Hammarlund, E.U., Haxen, E.R., Su, J., Wang, Y., Canfield, D.E., 2017. Oxygen, climate and the chemical evolution of a 1400 million year old tropical marine setting. Am. J. Sci. 317 (8), 861–900.
- Wang, X.Q., Jiang, G.Q., Shi, X.Y., Peng, Y.B., Morales, D.C., 2018. Nitrogen isotope

constraints on the early Ediacaran ocean redox structure. Geochim. Cosmochim. Acta 240, 220–235.

- Wang, Z.P., Wang, X.Q., Shi, X.Y., Tang, D.J., Stüeken, E.E., Song, H.Y., 2020b. Coupled Nitrate and Phosphate Availability Facilitated the Expansion of Eukaryotic Life at Circa 1.56 Ga. J. Geophys. Res. Biogeosci. 125, 1–17.
- Yang, S., Kendall, B., Lu, X.Z., Zhang, F.F., Zheng, W., 2017. Uranium isotope compositions of mid-Proterozoic black shales: evidence for an episode of increased ocean oxygenation at 1.36Ga and evaluation of the effect of post-depositional hydrothermal fluid flow. Precambrian Res. 298, 187–3201.
- Young, G.M., 2013. Precambrian supercontinents, glaciations, atmospheric oxygenation, metazoan evolution and an impact that may have changed the second half of Earth history. Geosci. Front. 4, 247–261.
- Zerkle, A., Junium, C.K., Canfield, D.E., House, C.H., 2008. Production of ^{15}N-depleted biomass during cyanobacterial N_2-fixation at high Fe concentrations. J. Geophys. Res. Biogeosci. 113, G03014.
- Zhang, K., Zhu, X.K., Wood, R.A., Shi, Y., Gao, Z.F., Poulton, S.W., 2018. Oxygenation of the Mesoproterozoic ocean and the evolution of complex eukaryotes. Nat. Geosci. 11, 345–350.
- Zhang, Q.X., 2020. Analysis of the source-reservoir characteristics of the middle-upper proterozoic shale gas in Kuancheng District. Coal and Chemical Industry. 43, 105–110 (in Chinese with English summary).
- Zhang, S.C., Su, J., Ma, S.H., Wang, H.J., Wang, X.M., He, K., Wang, H.T., Canfield, D.E., 2021. Eukaryotic red and green algae populated the tropical ocean 1400 million years ago. Precambrian Res. 357, 0301–9268.
- Zhang, S.C., Wang, X.M., Hammarlund, E.U., Wang, H.J., Costa, M.M., Bjerrum, C.J., Connelly, J.N., Zhang, B.M., Bian, L.Z., Canfield, D.E., 2015. Orbital forcing of climate 1.4 billion years ago. Proc. Natl. Acad. Sci. U.S.A. 113(7), 1731–1736.
- Zhang, S.C., Wang, X.M., Wang, H.J., Bjerrum, C.J., Hammarlund, E.U., Costa, M.M., Connelly, J.N., Zhang, B.M., Su, J., Canfield, D.E., 2016. Sufficient oxygen for animal respiration 1,400 million years ago. Proc. Natl. Acad. Sci. U.S.A. 113, 1731–1736.
- Zhang, X.N., Sigman, D.M., Morel, F.M.M., Kraepiel, A.M.L., 2014. Nitrogen isotope fractionation by alternative nitrogenases and past ocean anoxia. Proc. Natl. Acad. Sci. U.S.A.111 (13), 4782–4787.
- Zhu, S.X., Zhu, M.Y., Knoll, A.H., Yin, Z.J., Zhao, F.C., Sun, S.F., Qu, Y.G., Shi, M., Liu, H., 2016. Decimetre-scale multicellular eukaryotes from the 1.56-billion-year-old Gaoyuzhuang Formation in North China. Nat. Commun. 7, 11500.

Figure captions

Fig. 1. (A) Paleogeography of the Yanliao Basin during the Mesoproterozoic (modified

after Shi et al., 2021), showing the locations of the sampling drilling. (B) Location of the Yanliao Basin in the North China Craton (red box). (C) Generalized Paleo- and Mesoproterozoic stratigraphic sequence in the Yanliao Basin, North China Craton, with key tectonic events and geochronological data (modified after Wang et al., 2017, with age data from references therein). (D) Stratigraphic column of the XML Fm. in drill CQ-2 with sampling records. (E) Stratigraphic column of the HSZ Fm. in drill CQ-1 with sampling records.

Fig. 2. The percentage of Fe_{carb}, Fe_{ox}, Fe_{mag}, and Fe_{py} in Fe_{HR} pool for each sample.

Fig. 3. Stratigraphic profiles of redox proxies of the HSZ Fm. and the XML Fm. in drill CQ-1 and drill CQ-2, respectively. Vertical dash line(s) distinguish oxic ($Fe_{HR}/Fe_T < 0.22$) from equivocal ($Fe_{HR}/Fe_T = 0.22$–0.38) and anoxic ($Fe_{HR}/Fe_T > 0.38$) conditions in the Fe_{HR}/Fe_T profile, differentiates the ferruginous ($Fe_{py}/Fe_{HR} < 0.7$) from euxinic ($Fe_{py}/Fe_{HR} > 0.7$) conditions in the Fe_{HR}/Fe_T profile, seperates the non-euxinic from euxinic conditions in the Mo profile, discriminates RSE deleption from enrichment relative to UCC level in the RSE EFs profiles, and discernes Mo deleption from enrichment relative to U in the Mo/U $_{(EF)}$ profile.

Fig. 4. Stratigraphic profiles of TOC and TN contents, C/N ratios and $\delta^{15}N$ values of the HSZ Fm. and XML Fm. in drill CQ-1 and drill CQ-2, respectively. Vertical red dash lines represent the Redfield values in modern ocean (Redfield, 1934).

Fig. 5. Cross-plots showing the relationship of (A) TN versus TOC, (B) $\delta^{15}N$ versus TOC, (C) $\delta^{15}N$ versus TN, and (D) $\delta^{15}N$ versus molar C/N ratio for the studied HSZ and XML sections.

Fig. 6. Box plots of nearshore and offshore $\delta^{15}N$ data in Mesoproterozoic basins with p-values of student's t-test performed, reflecting an onshore to offshore nitrate gradient. n represents the numbers of the samples compiled. Data source: Yanliao Basin from Luo et al. (2015), Wang et al.(2020b), Shi et al. (2021), Zhang et al. (2021) and this study, Bangemall and Roper basins from Koehler et al. (2017), Belt basin from Stüeken (2013).

Fig. 7. Compilation of sedimentary $\delta^{15}N$ data through the Mesoproterozoic with data from ~1560Ma, ~1460 Ma and ~1380 Ma Yanliao Basin, China (Luo et al., 2015; Wang et al., 2020b; Shi et al., 2021; Zhang et al., 2021 and this study), ~1500Ma Bangemall basin and ~1450 Ma Roper Basin, Australia (Koehler et al., 2017), ~1400 Ma Belt Basin, USA (Stüeken, 2013), ~1200 Ma Vindhyan Basin, India (Gilleaudeau et al., 2020), ~1100 Ma Paranoá Group, Brazil (Stüeken et al., 2021) and ~1048 Ma Borden Basin, Canada (Hodgskiss et al., 2020). The orange area represents the typical range of nitrogen fixation. The fossil and biomarker records during the Mesoproterozoic are from Fairchild et al. (1996), Buick and Knoll (1999), Javaux et al. (2001), Zhu et al. (2016), Miao et al. (2021), Zhang et al. (2021). n represents the numbers of the
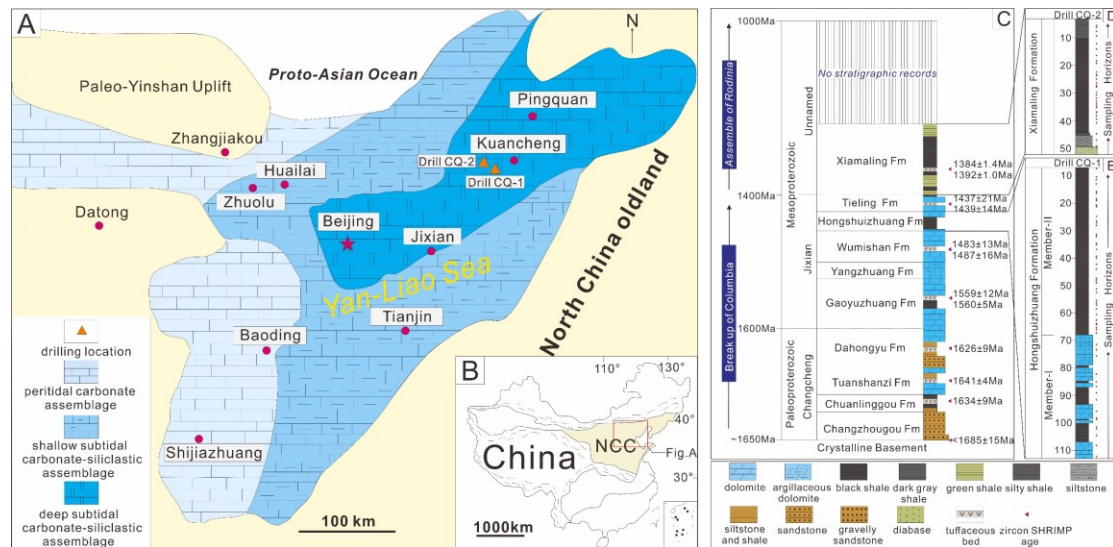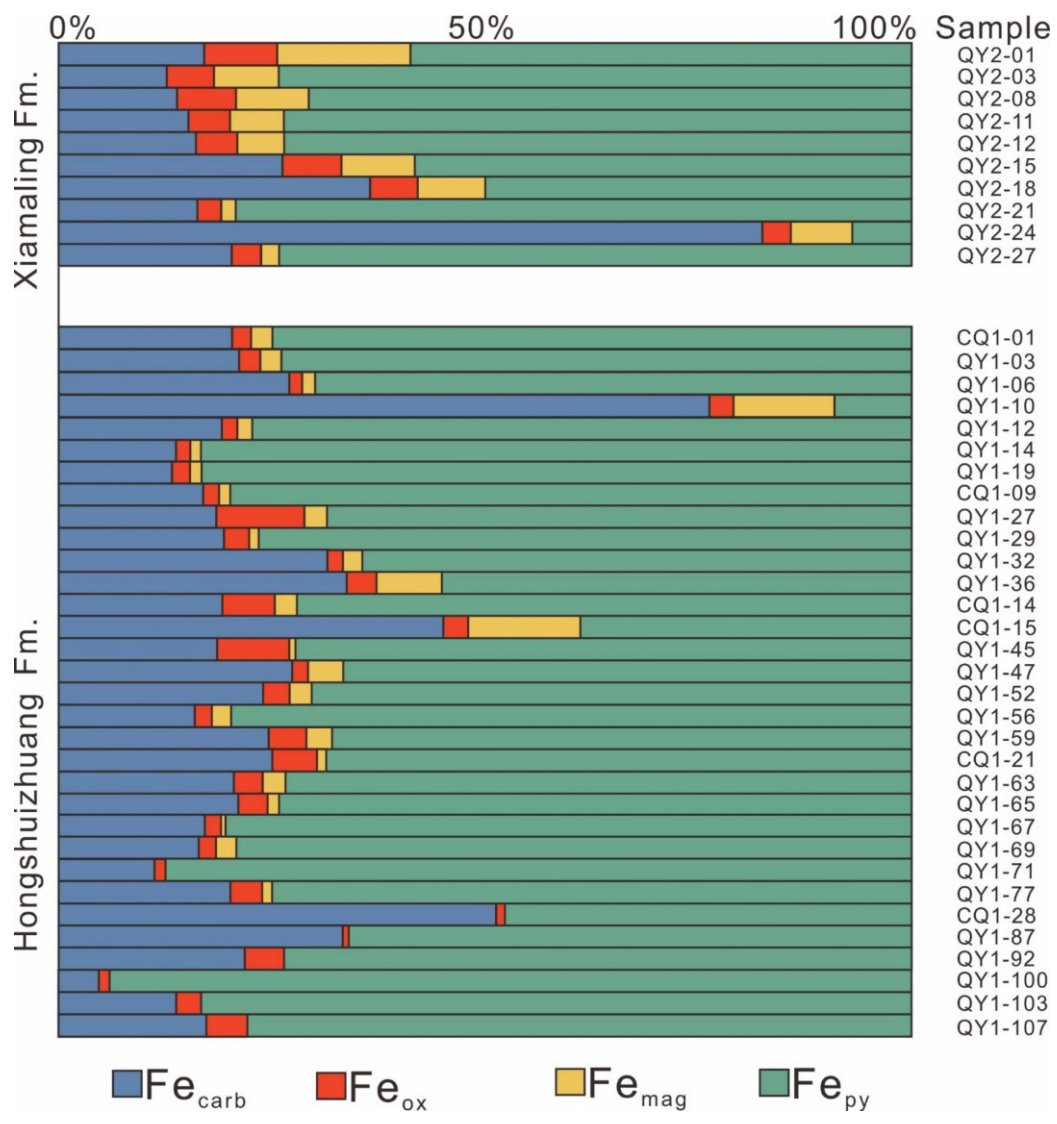
samples compiled.

Fig. 1. (A) Paleogeography of the Yanliao Basin during the Mesoproterozoic (modified after Shi et al., 2021), showing the locations of the sampling drilling. (B) Location of the Yanliao Basin in the North China Craton (red box). (C) Generalized Paleo- and Mesoproterozoic stratigraphic sequence in the Yanliao Basin, North China Craton, with key tectonic events and geochronological data (modified after Wang et al., 2017, with age data from references therein). (D) Stratigraphic column of the XML Fm. in drill CQ-2 with sampling records. (E) Stratigraphic column of the HSZ Fm. in drill CQ-1 with sampling records.

Fig. 2. The percentage of Fe_{carb}, Fe_{ox}, Fe_{mag}, and Fe_{py} in Fe_{HR} pool for each sample.
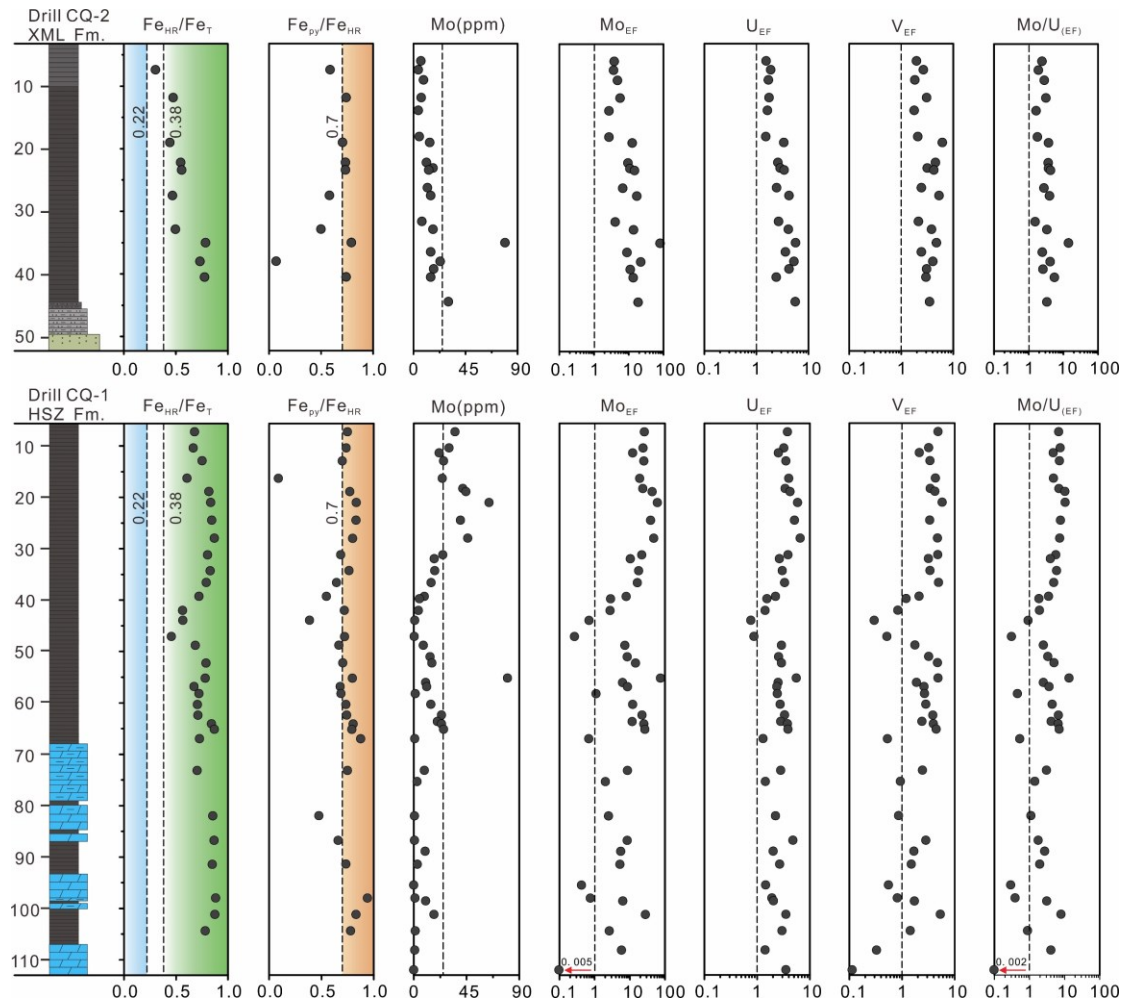
Fig. 3. Stratigraphic profiles of redox proxies of the HSZ Fm. and the XML Fm. in drill CQ-1 and drill CQ-2, respectively. Vertical dash line(s) distinguish oxic ($Fe_{HR}/Fe_T <$ 0.22) from equivocal (Fe_{HR}/Fe_T = 0.22–0.38) and anoxic ($Fe_{HR}/Fe_T >$ 0.38) conditions in the Fe_{HR}/Fe_T profile, differentiates the ferruginous ($Fe_{py}/Fe_{HR} <$ 0.7) from euxinic ($Fe_{py}/Fe_{HR} >$ 0.7) conditions in the Fe_{HR}/Fe_T profile, seperates the non-euxinic from euxinic conditions in the Mo profile, discriminates RSE deleption from enrichment relative to UCC level in the RSE EFs profiles, and discernes Mo deleption from enrichment relative to U in the Mo/U $_{(EF)}$ profile.
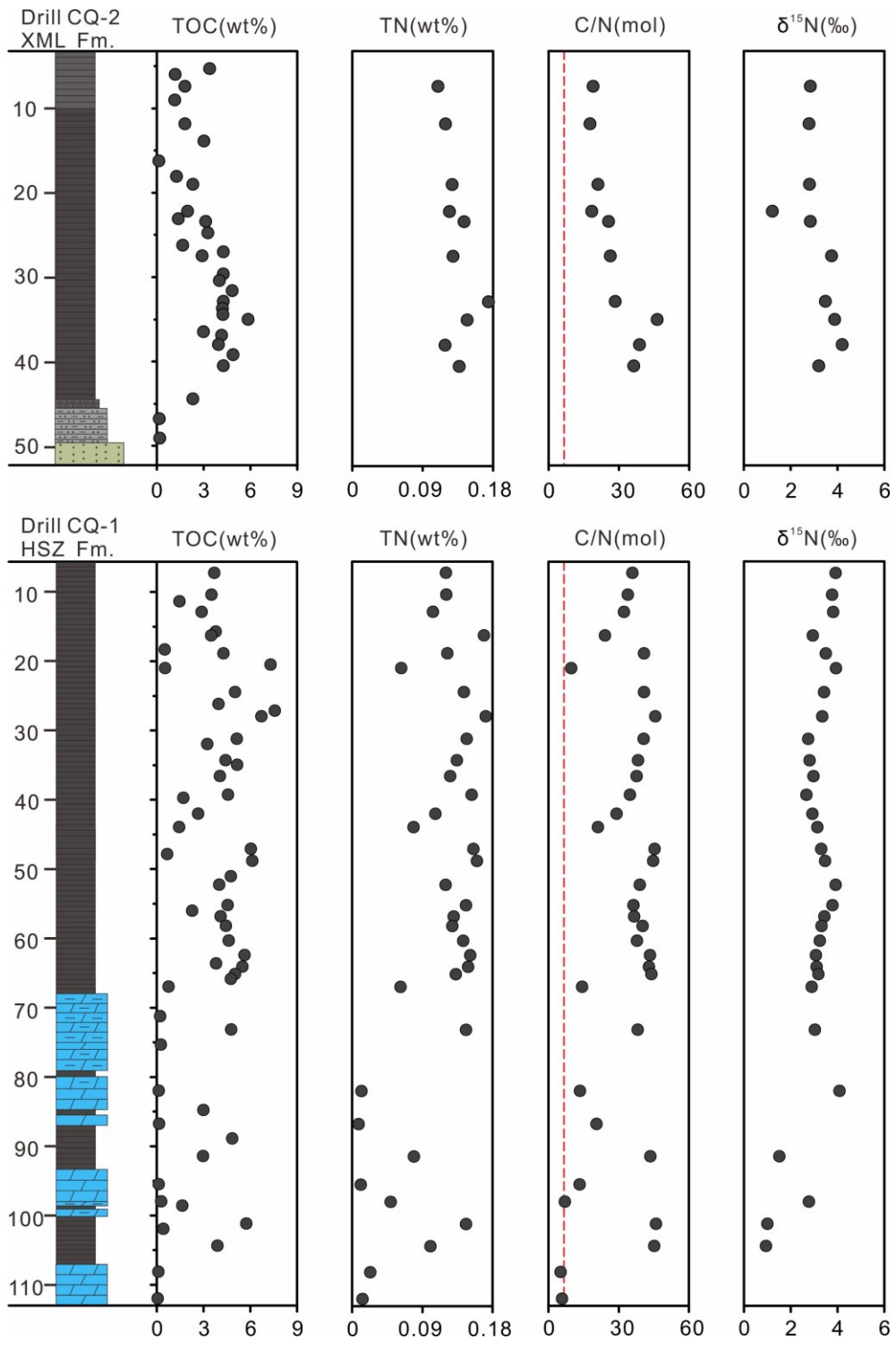
Fig. 4. Stratigraphic profiles of TOC and TN contents, C/N ratios and δ^{15}N values of the HSZ Fm. and XML Fm. in drill CQ-1 and drill CQ-2, respectively. Vertical red dash lines represent the Redfield values in modern ocean (Redfield, 1934).
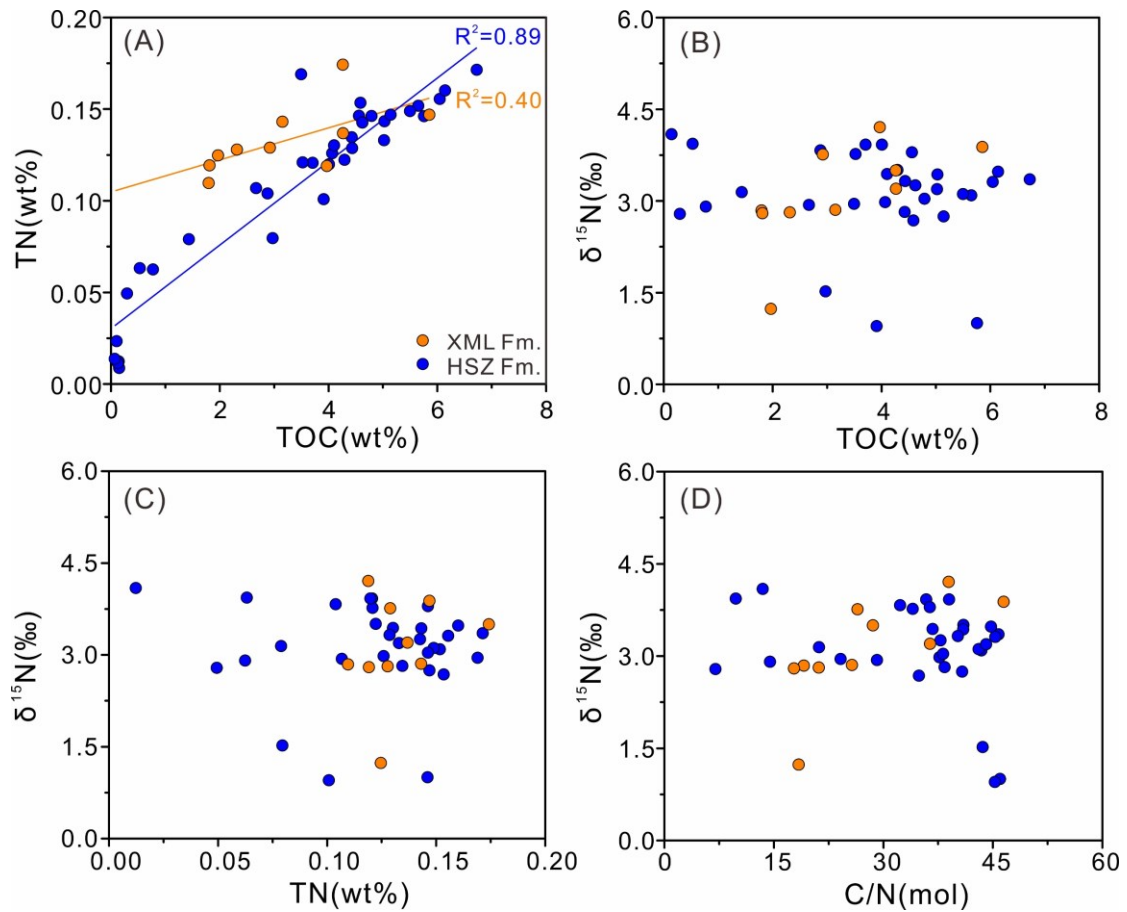
Fig. 5. Cross-plots showing the relationship of (A) TN versus TOC, (B) $\delta^{15}N$ versus TOC, (C) $\delta^{15}N$ versus TN, and (D) $\delta^{15}N$ versus molar C/N ratio for the studied HSZ and XML sections.
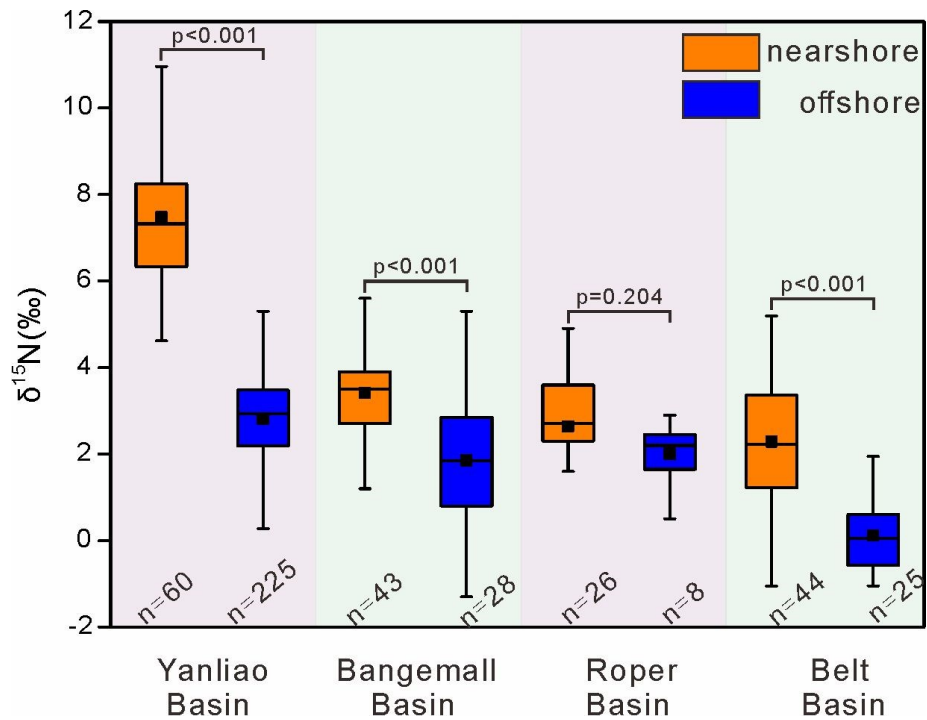
Fig. 6. Box plots of nearshore and offshore $\delta^{15}N$ data in Mesoproterozoic basins with p-values of student's t-test performed, reflecting an onshore to offshore nitrate gradient. n represents the numbers of the samples compiled. Data source: Yanliao Basin from Luo et al. (2015), Wang et al.(2020b), Shi et al. (2021), Zhang et al. (2021) and this study, Bangemall and Roper basins from Koehler et al. (2017), Belt basin from Stüeken (2013).
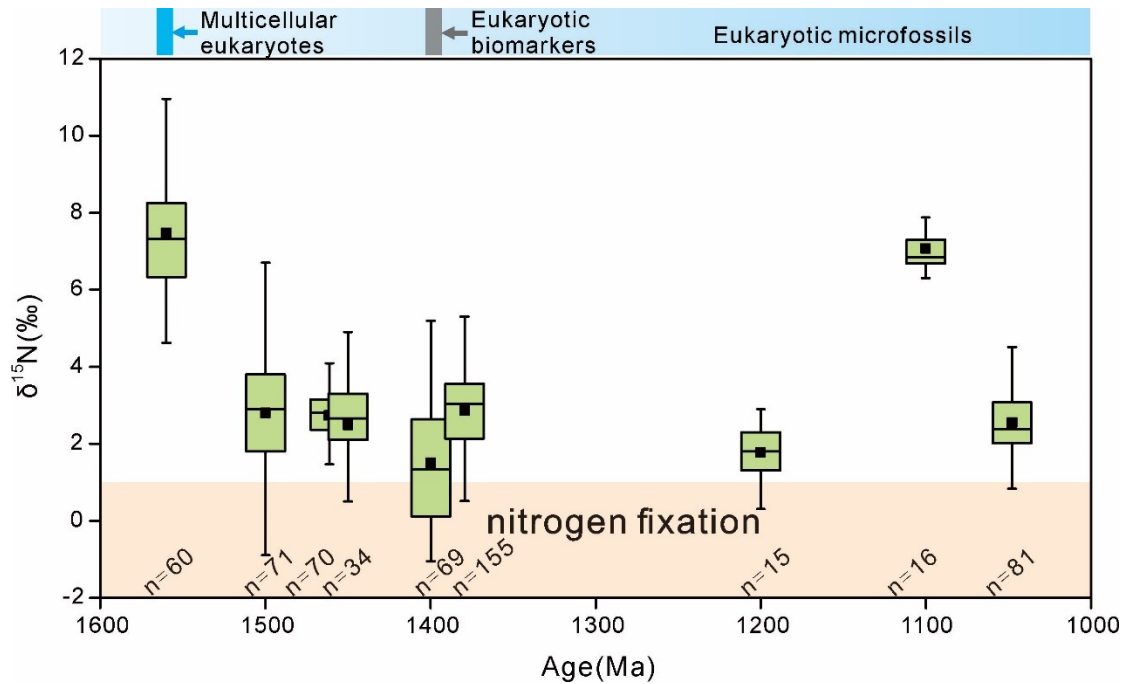
Fig. 7. Compilation of sedimentary $\delta^{15}N$ data through the Mesoproterozoic with data from ~1560Ma, ~1460 Ma and ~1380 Ma Yanliao Basin, China (Luo et al., 2015; Wang et al., 2020b; Shi et al., 2021; Zhang et al., 2021 and this study), ~1500Ma Bangemall basin and ~1450 Ma Roper Basin, Australia (Koehler et al., 2017), ~1400 Ma Belt Basin, USA (Stüeken, 2013), ~1200 Ma Vindhyan Basin, India (Gilleaudeau et al., 2020), ~1100 Ma Paranoá Group, Brazil (Stüeken et al., 2021) and ~1048 Ma Borden Basin, Canada (Hodgskiss et al., 2020). The orange area represents the typical range of nitrogen fixation. The fossil and biomarker records during the Mesoproterozoic are from Fairchild et al. (1996), Buick and Knoll (1999), Javaux et al. (2001), Zhu et al. (2016), Miao et al. (2021), Zhang et al. (2021). n represents the numbers of the samples compiled.